Journal of the Taiwan Institute of Chemical Engineers 132 (2022) 104110

Contents lists available at ScienceDirect

Journal of the Taiwan Institute of Chemical Engineers

journal homepage: www.elsevier.com/locate/jtice

Solid state chemical transformations through ring-opening polymerization of ferrocene-based conjugated microporous polymers in host−guest complexes with benzoxazine-linked cyclodextrin

Maha Mohamed Samy[a,b,1], Mohamed Gamal Mohamed[a,b,1], Tharwat Hassan Mansoure[b], Tso Shiuan Meng[a], Mo Aqib Raza Khan[c], Chih-Chuang Liaw[c], Shiao-Wei Kuo[a,d,*]

[a] Department of Materials and Optoelectronic Science, Center of Crystal Research, National Sun Yat-Sen University, Kaohsiung 80424, Taiwan
[b] Chemistry Department, Faculty of Science, Assiut University, Assiut 71516, Egypt
[c] Department of Marine Biotechnology, National Sun Yat-sen University, Kaohsiung 80424, Taiwan
[d] Department of Medicinal and Applied Chemistry, Kaohsiung Medical University, Kaohsiung 807, Taiwan

ARTICLE INFO

Article History:
Received 17 August 2021
Revised 26 September 2021
Accepted 6 October 2021
Available online 20 October 2021

Keywords:
Conjugated microporous polymer
Host-guest complex
Benzoxazine
Cyclodextrin
CO_2 uptake

ABSTRACT

Herein, we describe two ferrocene-derived conjugated microporous polymers (FFC—CMPs) prepared through Sonogashira couplings of 9-ferrocenylidene-2,7-dibromo-9*H*-fluorene (FFC) with tetraethynylpyrene (Py-T) and tetrakis(4-ethynylphenyl)ethene (TPE-T), respectively, and their properties determined using various spectroscopic techniques. These two FFC CMPs formed inclusion complexes (ICs) with a benzoxazine-linked β-cyclodextrin (CD-BZ), with host-guest interactions occurring between the ferrocene and β-CD units. We used Fourier transform infrared spectroscopy, X-ray diffraction, two-dimensional nuclear Overhauser enhancement NMR spectroscopy, solid-state ^{13}C CP/MAS NMR spectroscopy, and thermogravimetric analysis to characterize these FFC—CMP/CD-BZ ICs. The BZ units in the FFC—CMP/CD-BZ ICs underwent thermal ring-opening polymerization to form new Mannich bridges featuring both intermolecular (OH···O) and intramolecular (OH···N) hydrogen bonds; the resulting TPE-FFC—CMP/poly(CD-BZ) and Py-FFC—CMP/poly (CD-BZ) ICs exhibited outstanding thermal stability, with the latter having the higher CO_2 uptake ability (1.42 mmol g^{-1}) and capacitance (46 F g^{-1} at 0.5 A g^{-1}).

Background: Host−guest complexes formed from macrocyclic hosts possessing hydrophobic cavities such as cyclodextrins (CDs) and various guest molecules have been studied widely for their fascinating characteristics. The interaction of ferrocene-containing CMPs with hydrophobic cavities of CDs to form inclusion complexes materials with excellent thermal properties and these materials can be used in different fields including energy storage and gas capture.

Methods: Two ferrocene-based fluorene CMPs—TPE-FFC CMP and Py-FFC—CMP—through Sonogashira couplings of 9-ferrocenylidene-2,7-dibromo-9*H*-fluorene (FFC), as the main block, with tetraethynylpyrene (Py-T) and tetrakis(4-ethynylphenyl)ethene (TPE-T), were successfully synthesized through Sonogashira couplings. Then, the two FFC CMPs were attached to a benzoxazine-functionalized β-cyclodextrin (CD-BZ) through host-guest complexation. The successful synthesis of two FFC CMPs and FFC—CMP/CD-BZ ICs was investigated by using Fourier transform infrared spectroscopy, X-ray diffraction, two-dimensional nuclear Overhauser enhancement NMR spectroscopy, solid-state ^{13}C CP/MAS NMR spectroscopy, and thermogravimetric analysis.

Significant Findings: The present work offers a new and facile strategy for the preparation CMPs/CD inclusion complexes through supramolecular chemistry and using these materials as an electrode in the energy devices and CO_2 uptake.

1. Introduction

Conjugated microporous polymers (CMPs) are an emerging class of porous materials having extended conjugated skeletons in their polymeric frameworks. They are attractive because of their wide applicability in several fields, including supercapacitors, metal-ion

* Corresponding author at: Department of Materials and Optoelectronic Science, Center of Crystal Research, National Sun Yat-Sen University, Kaohsiung 80424, Taiwan
E-mail address: kuosw@faculty.nsysu.edu.tw (S.-W. Kuo).
[1] These authors contributed equally to this work.

https://doi.org/10.1016/j.jtice.2021.10.010
1876-1070/

batteries, hydrogen evolution, energy storage, fuel cells, sensors, photocatalysis, phototherapy, CO_2 adsorption, and optoelectronics [1–18]. CMPs can be prepared—with a range of microporous morphologies presenting various molecular structures of conjugated polymers—using a variety of synthetic methods, including Heck reactions, Schiff-base formation, oxidative coupling, Sonogashira coupling, cyclotrimerization, Yamamoto and Suzuki coupling [19–27]. The diversity of CMP structures leads to many having attractive properties, including high conductivities, mechanical rigidities, surface areas, porosities, and thermal stabilities. Interestingly, solid-state chemical transformations of CMPs have been performed without changing their topologies significantly, typically through post-modification of the linkages of the CMPs. For example, imine-linked CMPs have been converted to secondary amides, secondary amines, oxazoles, thiazoles, and quinolones; as a result, amide- and oxazole-linked CMPs can be synthesized from their building blocks directly [28–36]. In addition, cyclic carbamate- and thiocarbamate-linked CMPs have been obtained from imine-linked CMPs through multistep post-modifications in the solid state, retaining the high surface areas (>780 $m^2\ g^{-1}$) and long-range order of the crystalline and porous structures of their precursors [37].

Benzoxazine (BZ) units undergo ring-opening polymerization (ROP) to form polybenzoxazines (PBZs) featuring strong intramolecular (OH···N) and intermolecular (OH···O) hydrogen bonds, thereby enhancing the thermal stabilities and dielectric constants [38–46]. In previous studies, we synthesized porous organic polymers featuring BZ-linkages through direct one-pot Mannich reactions and multistep syntheses using tetraphenylethylene (TPE) as the building block [47,48]. We performed post-modifications of the linkages of these CMPs through the formation of covalent bonds; to the best of our knowledge, noncovalent bonding has not been reported previously to introduce BZ-linkages into CMPs.

Supramolecular interactions are exploited in many different fields, including catalysis, biochemistry, organic synthesis, and electronics. They involve various types of intermolecular noncovalent bonding, typically van der Waals interactions, metal coordination, hydrophobic interactions and π-stacking [49–52]. Host–guest complexes formed from macrocyclic hosts possessing hydrophobic cavities [e.g., cyclodextrins (CDs), calixarenes, and cyclophanes] and various guest molecules have been studied widely for their fascinating characteristics [53, 54]. By allowing noncovalent interactions to exist between their components, various supramolecular host-guest inclusion complexes (ICs) can be formed in a facile manner for practical use. CDs are among the most popular macrocyclic receptors used to introduce supramolecular interactions; they are cyclic oligomers of α–1,4-D-glucopyranose, with α-, β-, and γ-CD being most common, differentiated by their ring sizes. The hydrophobic cavities of CDs interact with various guest molecules, including azobenzene, polyethylene glycol, adamantane, and ferrocene units, forming ICs [55,56]. β-CD has been the most widely used of the CDs because of its commercial availability, unique structure, outstanding biocompatibility, and facile chemical modification [55]. Ferrocene units can be incorporated into the hydrophobic cavity of β-CD through supramolecular hydrophobic interactions, forming ICs of equal mole ratio. For example, Yuan *et al.* prepared supramolecular graft copolymers featuring host–guest interactions between β-CD in the main chain and ferrocene units and investigated their responsiveness for electrochemical redox applications [57]. Guo et al. obtained amphiphilic polymers from β-CD dextran and a ferrocene-terminated polycaprolactam, based on a host–guest strategy; they used cyclic voltammetry (CV) and two-dimensional (2D) NMR spectroscopy to confirm the presence of the ICs formed between the two units [58]. Ni and coworkers fabricated a graft copolymer (Dex-β-CD/Fc-PLA) through host–guest complexation of building blocks featuring ferrocene and β-CD moieties [59].

The introduction of organometallic compounds (in particular, ferrocene) in the skeletons of CMPs can lead to excellent electrical, optical, sensing, catalytic, magnetic, thermal, and redox properties. Indeed, ferrocene-containing CMPs have been used in various applications, including gas storage, lithium batteries, dye removal, catalysis, magnetic switches, and memory devices [60–67]. For example, Liu et al. used Yamamoto coupling to prepare two ferrocene-based CMPs displaying good thermal stability and gas storage capacity [68]. Wong et al. synthesized ferrocene-based hyperbranched polymers through Sonogashira coupling of 9-ferrocenylidene-2,7-diiodo-9*H*-fluorene and tri(4-ethynylphenyl)amine; by controlling the morphology of these synthesized polymers, they obtained nanostructures suitable for use in water treatment and lithium-ion batteries [69].

In this study, we synthesized two ferrocene-based fluorene CMPs—TPE-FFC CMP and Py-FFC—CMP—through Sonogashira couplings of 9-ferrocenylidene-2,7-dibromo-9*H*-fluorene (FFC), as the main block, with tetraethynylpyrene (Py-T) and tetrakis(4-ethynylphenyl)ethene (TPE-T), respectively [Schemes 1(a) and 1(b)]. We then attached the two FFC CMPs to a benzoxazine-functionalized β-cyclodextrin (CD-BZ) [70] through host–guest complexation of the β-CD and ferrocene moieties to form FFC/CD-BZ CMP ICs [Schemes 1 (c) and 1(d)]. The formation of the ICs between the FFC—CMPs and β-CD was confirmed using 2D nuclear Overhauser enhancement (2D NOESY) NMR spectroscopy. To the best of our knowledge, these FFC—CMP/CD-BZ ICs are the first examples of CMPs possessing BZ units introduced through host–guest interaction of FFC and β-CD units; furthermore, these BZ units underwent ROP upon thermal treatment, without the need for a catalyst or curing agent [52].

2. Experimental

2.1. Materials

Potassium hydroxide (KOH), triphenylphosphine (PPh_3), and copper iodide (CuI) were purchased from Alfa Aesar. Tetrakis(triphenylphosphine)palladium(0) [$Pd(PPh_3)_4$] was obtained from Sigma–Aldrich. Ethanol (EtOH), triethylamine (Et_3N), and *N,N*-dimethylformamide (DMF), methanol (MeOH), tetrahydrofuran (THF), and ferrocene carboxaldehyde were obtained from Acros. Tetrakis(4-bromophenyl)ethylene (TPE-Br_4), 1,3,6,8-tetrabromopyrene (Py-Br_4), 2,7-dibromo-9*H*-fluorene (F-Br_2), 1,3,6,8-tetraethynylpyrene (Py-T) 1,1,2,2-tetrakis(4-ethynylphenyl)ethene (TPE-T), FPy-CMP, and CD-BZ (Scheme S2) were prepared using previously reported procedures [1,16,48,70-74].

2.2. FTPE-CMP

A solution of PPh_3 (6.0 mg, 0.023 mmol), $Pd(PPh_3)_4$ (27 mg, 0.023 mmol), F-Br_2 (0.15 g, 0.46 mmol), TPE-T (0.10 g, 0.23 mmol), and CuI (4.0 mg, 0.023 mmol) in dry DMF and Et_3N (14 mL) was degassed (using vacuum pump and N_2) and then heated under reflux at 110 °C (oil bath) for 3 days. The orange precipitate was filtered off, washed thoroughly with DMF, MeOH, and THF, and then dried in an oven for 2 days [Scheme S1(a)]. FTIR (KBr, cm^{-1}): 3059 (aromatic C–H stretching), 2191 (C≡C stretching), 1601 (C=C stretching) [Figure S1(a)].

2.3. FPy-CMP

A solution of $Pd(PPh_3)_4$ (27 mg, 0.023 mmol), F-Br_2 (0.15 g, 0.46 mmol), PPh_3 (6.0 mg, 0.023 mmol), Py-T (0.1 g, 0.23 mmol), and CuI (4.0 mg, 0.023 mmol) in dry DMF and Et_3N (14 mL) was degassed (using a vacuum pump and N_2) and then heated under reflux at 110 °C (oil bath) for 3 days. The orange precipitate was filtered off, washed thoroughly with DMF, MeOH, and THF, and then dried in an oven for 2 days [Scheme S1(b)]. FTIR (KBr, cm^{-1}): 3059 (aromatic C–H stretching), 2191 (C≡ C stretching), 1601 (C=C stretching) [Figure S1(b)].

2.4. 9-Ferrocenylidene-2,7-dibromo-9H-fluorene (FFC)

A mixture of F-Br_2 (0.80 g), KOH (0.27 g), and ferrocene carboxaldehyde (0.58 g) in EtOH (50 mL) was heated under reflux at 70 °C for 24 h. The red precipitate was washed with EtOH and dried in an oven at 80 °C for 24 h (Scheme 1). FTIR (KBr, cm^{-1}): 3095 (aromatic C–H stretching). ^{1}H NMR (500 MHz, $CDCl_3$, δ, ppm, Figure S2): 8.40, 7.88, 7.56, 7.56, 7.46, 4.72, 4.56, 4.26. ^{13}C NMR (125 MHz, $CDCl_3$, δ, ppm, Figure S3): 141.6, 138.4, 138.3, 135.9, 131, 130.5, 130.1, 129.7, 127, 122.8, 121, 120.9, 120.6, 80, 70.9, 70.6, 69.7. (+)ESI-MS: *m/z* 521 ($C_{23}H_{16}FeBr_2$) (Figure S4).

2.5. TPE-FFC—CMP

A solution of CuI (8.0 mg, 0.040 mmol), FFC (0.24 g, 0.46 mmol), Pd$(PPh_3)_4$ (50 mg, 0.045 mmol), TPE-T (0.10 g, 0.23 mmol), and PPh_3 (12 mg, 0.050 mmol) in dry DMF and Et_3N (14 mL) was degassed (using a vacuum pump and N_2) and then heated under reflux at 110 °C (oil bath) for 3 days. The brown solid was filtered off and washed thoroughly with DMF, MeOH, and THF. FTIR (KBr, cm^{-1}): 3095 (aromatic C–H stretching), 2197 (C≡C stretching), 1628 (C=C stretching) [Fig. 1(b)].

2.6. Py-FFC—CMP

This CMP was prepared as a dark-red precipitate by using the procedure described above for TPE-FFC—CMP, but with the following changes: PPh_3 (20 mg, 0.060 mmol), FFC (0.34 g, 0.66 mmol), Py-T (0.10 g, 0.33 mmol), and CuI (0.01 g, 0.05 mmol). FTIR (KBr, cm^{-1}): 3095 (aromatic C–H stretching), 2197 (C≡C stretching), 1628 (C=C stretching) [Fig. 1(c)].

2.7. CD-BZ/FFC and FFC/cd-BZ CMP ICs and thermal curing polymerization

CD-BZ (0.1 g) and FFC, Py-FFC—CMP, or TPE-FFC—CMP (0.05 g) were placed in distilled water (10 mL) and then the mixture was sonicated for 2 h and stirred for 12 h to form the CD-BZ/FFC and FFC/CD-BZ CMP ICs, respectively. Each FFC/CD-BZ CMP IC (0.15 g) was then

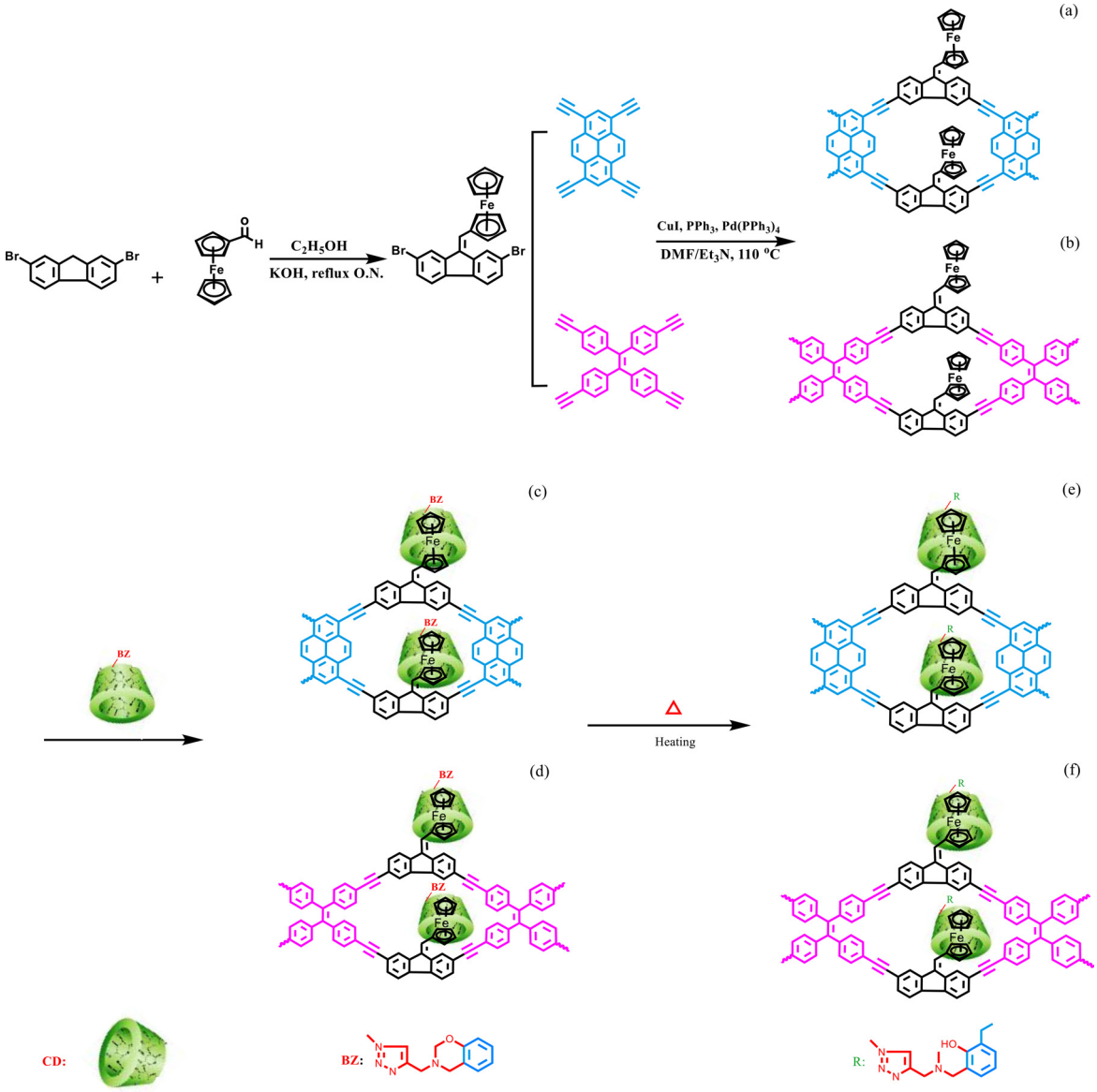

Scheme 1. Schematic representations of (a) Py-FFC—CMP, (b) TPE-FFC—CMP, (c) Py-FFC/CD-BZ CMP, (d) TPE-FFC/CD-BZ CMP, (e) Py-FFC/CD-BZ CMP after curing, and (f) TPE-FFC/CD-BZ CMP after curing.

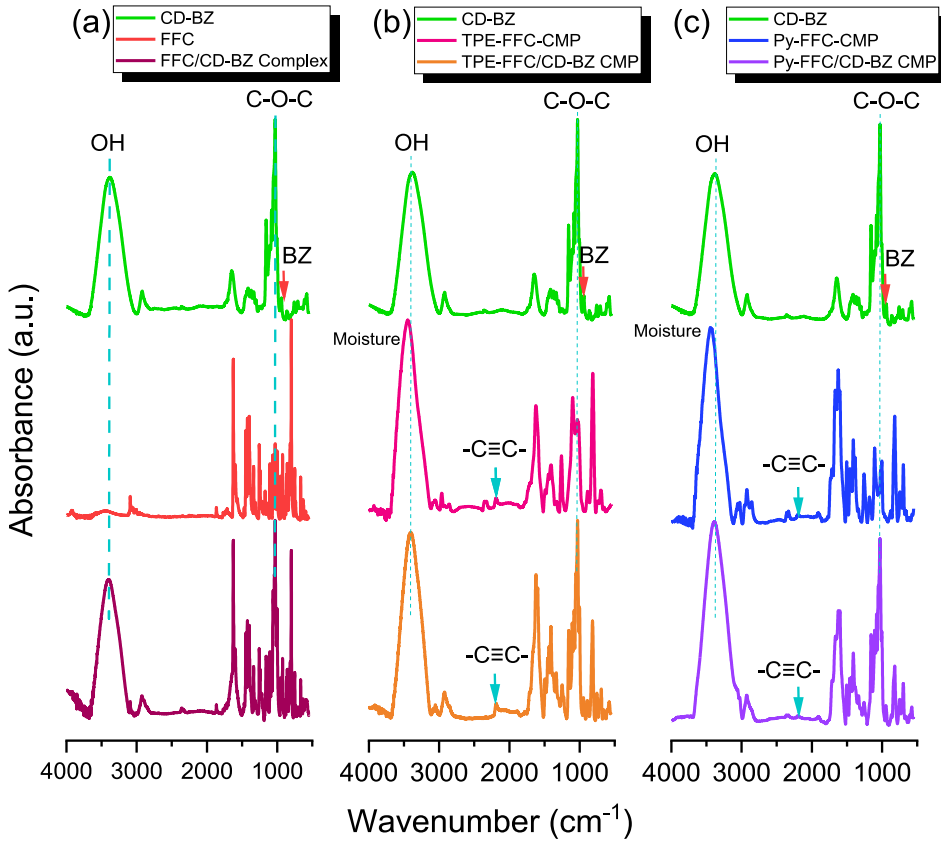

Fig. 1. FTIR spectra of (a) CD-BZ, FFC, and the FFC/CD-BZ complex; (b) CD-BZ,TPE-FFC—CMP, and the TPE-FFC/CD-BZ CMP; and (c) CD-BZ, Py-FFC—CMP, and the Py-FFC/CD-BZ CMP.

cured at 300 °C for 4 h to afford the FFC/poly(CD-BZ) CMP as a dark-brown solid.

3. Results and discussion

3.1. Synthesis of FFC monomer

The FFC monomer was prepared through condensation of F-Br_2 and ferrocene carboxaldehyde in absolute EtOH in the presence of KOH (Scheme 1). The chemical structure of the FFC monomer was confirmed using conventional techniques (FTIR, ^{1}H and ^{13}C NMR, and FTMS spectroscopy; Figures S2–S4). The FTIR spectrum [Fig. 1(a)] featured a peak at 1628 cm^{-1} representing C=C stretching, but no characteristic peak for a carboxyl group, revealing that the condensation of F-Br_2 and ferrocene carboxaldehyde had given the target FFC monomer, isolated as a red solid. The ^{1}H NMR spectrum of the FFC monomer (Fig. S2) featured signals at 4.26, 4.56, and 4.72 ppm representing the Cp protons of the ferrocene moiety and at 7.46–7.88 and 8.40 ppm representing the aromatic and HC=C protons, respectively.

The ^{13}C NMR spectrum of the FFC monomer (Figure S3) featured peaks at 69.7, 70.6, 70.9, and 80.0 ppm representing the carbon nuclei of the Cp units, as well as signals at 120.6–138.4 and 141.6 ppm representing the carbon nuclei of the aromatic and HC=C units, respectively. The molecular weight of the FFC monomer (*m/z* 521), determined using (+)ESI mass spectrometry (Figure S4), was consistent with its expected calculated value (520.7).

3.2. Synthesis of Py-FFC-CMP and TPE-FFC-CMP

The two ferrocene-based fluorene conjugated microporous polymers (FFC—CMPs) were prepared through Sonogashira couplings of the FFC monomer with Py-T and TPE-T, respectively, in DMF/Et_3N with $Pd(PPh_3)_4$ as the catalyst [Schemes 1(a) and 1(b)]. The FTIR spectra of these two CMPs featured peaks at 2197 cm^{-1} for -C≡C- stretching and at 3095 cm^{-1} for C–H aromatic vibrations [Fig. 1(b) and 1(c)]. Fig. 2(b) and 2(d) present the solid-state ^{13}C CP/MAS NMR spectra of Py-FFC and TPE-FFC—CMPs with signal assignments. The peaks in the range from 69.2 to 92 ppm represented the alkyne and ferrocene units in both FFC—CMP frameworks; the signals at 120 and 129–140 ppm represent the carbon nuclei of the HC=C and aromatic units, respectively. These spectral data are consistent with the chemical structures of both FFC—CMPs.

We recorded Brunauer–Emmett–Teller (BET) isotherms at 77 K to investigate the porosities of FTPE-CMP, FPy-CMP, TPE-FFC—CMP, and Py-FFC—CMP (Fig. 3). The isotherms of FTPE-CMP [Fig. 3(a)] and FPy-CMP [Fig. 3(e)] reveal mesoporous structures for these CMP polymers (type IV according to IUPAC classification). The surface area (S_{BET}) and total pore volume (V_{total}) for FTPE-CMP were 31 $m^2\ g^{-1}$ and 0.06 $cm^3\ g^{-1}$, respectively; for FPy-CMP they were 191 $m^2\ g^{-1}$ and 0.17 $cm^3\ g^{-1}$, respectively. Nonlocal density functional theory (NL-DFT) revealed that the pore size distributions of FTPE-CMP and FPy-CMP were 1.24–2.37 [Fig. 3(b)] and 2.14–5.85 [Fig. 3(f)] nm, respectively. The TEM images in Fig. 3(c) and 3(g) reveals that these two CMPs were mesoporous with a few microporous structures having pore sizes of 1.5–2.5 nm. We suspect that the BET surface area and pore volume of FPy-CMP were higher than those of FTPE-CMP because a pyrene unit is more planar than a TPE unit, allowing the former to feature stronger π-stacking and a more ordered structure. After attaching ferrocene units to these two CMP polymers, TPE-FFC—CMP [Fig. 3(a)] and Py-FFC—CMP [Fig. 3(e)] provided similar type IV curves for their mesoporous structures; the values of S_{BET} and V_{total} decreased, however, to 8 $m^2\ g^{-1}$ and 0.04 $cm^3\ g^{-1}$, respectively, for TPE-FFC—CMP and to 50 $m^2\ g^{-1}$ and 0.07 $cm^3\ g^{-1}$, respectively, for Py-FFC—CMP. The pore size distributions were 0.47–2.83 nm for TPE-FFC—CMP [Fig. 3(b)] and 1.96–5.48 nm for Py-FFC—CMP [Fig. 3(f)], as confirmed through TEM imaging [Fig. 3(d) and 3(h)] of the

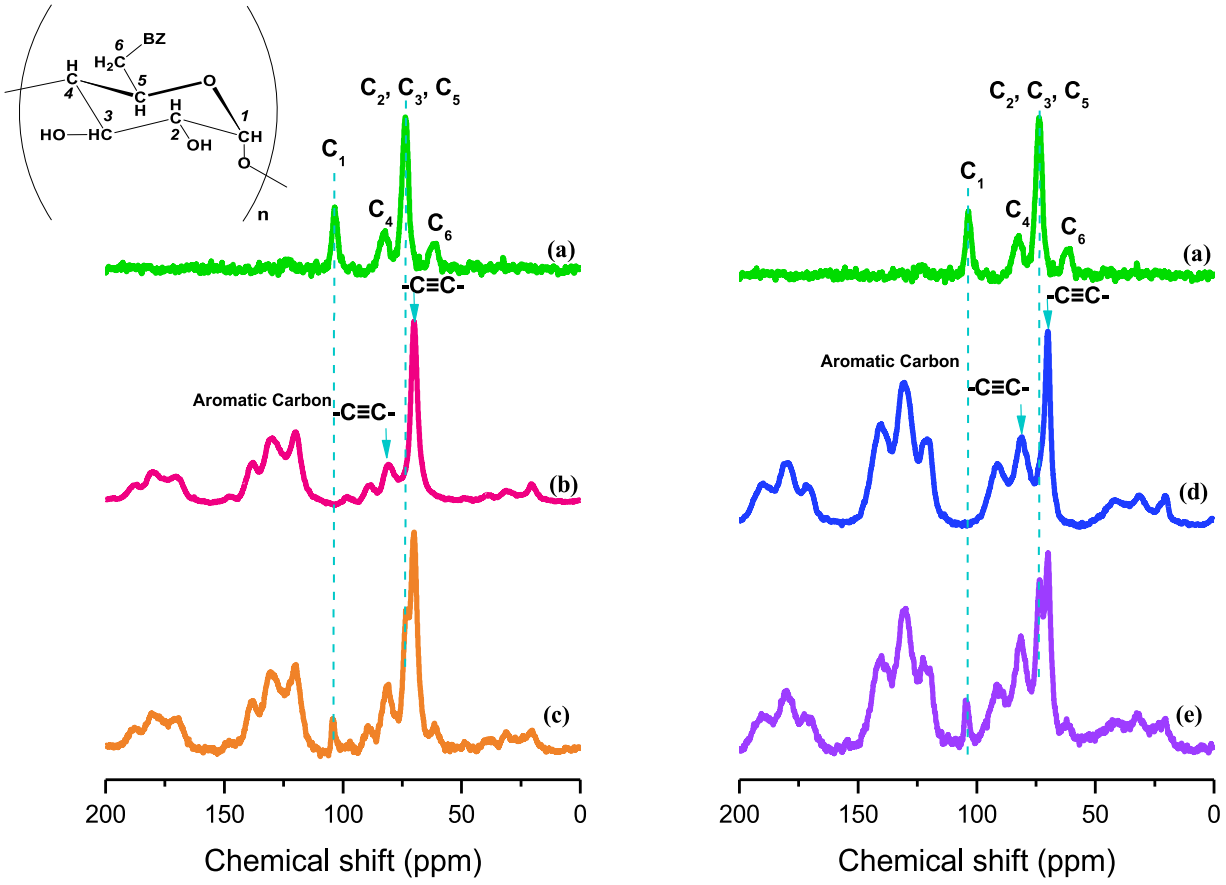

Fig. 2. ^{13}C NMR spectra of (a) CD-BZ, (b) TPE-FFC—CMP, (c) TPE-FFC/CD-BZ CMP, (d) Py-FFC—CMP, and (e) Py-FFC/CD-BZ CMP.

microporous structures. Thus, we suspect that the ferrocene units attached to these two CMP polymers as side groups occupied their porous spaces, thereby decreasing the surface areas and pore volumes. The hysteresis loops for all of the CMP materials were not closed because of the flexibility of the polymeric frameworks and their swelling through gas adsorption upon elastic deformation; this behavior has been observed for several CMPs [11,57].

Although the total pore volume and surface area both decreased after attaching the ferrocene units to these two CMPs, the thermal properties of TPE-FFC—CMP and Py-FFC—CMP both increased significantly, based on TGA measurements performed under N_2 at a heating rate of 20 °C min^{-1} (Fig. 4). For example, FTPE-CMP provided a value of T_{d10} of 357 °C and a char yield of 59.6 wt% at 800 °C, but these values increased significantly for TPE-FFC—CMP to 527 °C and 67.3 wt%, respectively. Furthermore, FPy-CMP provided a value of T_{d10} of 321 °C and a char yield of 53.2 wt% at 800 °C, but for Py-FFC—CMP they had increased significantly to 470 °C and 74.7 wt%, respectively. These values suggest outstanding thermal stability and rigidity for TPE-FFC—CMP and Py-FFC—CMP. Table 1 summarizes the BET and TGA data of these four CMP polymers.

Fig. 5 displays the X-ray diffraction (XRD) patterns of our two FFC—CMPs; weak diffraction peaks appeared at 13.3°, indicative of their amorphous structures. We used SEM (Figure S5) to study the morphologies of these two FFC—CMPs; the images revealed the aggregation of spherical structures.

3.3. Preparation and thermal curing polymerization of FFC/CD-BZ and FFC/CD-BZ CMP ICs

Because ferrocene forms an IC with β-CD, our FFC—CMPs readily underwent attachment of their ferrocene units through host–guest interactions with the water-soluble BZ-functionalized CD derivative CD-BZ in reasonable yield. The formation of the ICs was evidenced by the solution progressively becoming turbid; the uncomplexed CD-BZ was then removed by washing the ICs with acetone and water. To confirm that ICs could form between the FFC—CMPs and CD-BZ, we used 2D NOESY NMR spectroscopy to investigate the interaction of an equimolar mixture of the low-molecular-weight model compound FFC and CD-BZ (Fig. 6). Several NOE correlation peaks (green squares) existed between the signals of the protons H_3 and H_5 of CD-BZ and the signals of the protons of the substituent and Cp units (4.1–4.5 ppm) of FFC, consistent with a host–guest arrangement of FFC and CD-BZ. XRD, FTIR spectroscopy, TGA, and solid-state ^{13}C CP/MAS NMR spectroscopy provided further evidence for the formation of the FFC—CMP/CD-BZ ICs.

The FTIR spectra of the three ICs in Fig. 1 reveal signals for both CD-BZ and the FFC derivatives, implying that both components were present. The broad signal for the OH groups of CD-BZ near 3383 cm^{-1} was slightly shifted to 3396 cm^{-1} in the spectra of the ICs, consistent with the presence of host–guest complexation of CD-BZ and the FFC derivatives. Fig. 2 displays solid-state ^{13}C CP/MAS NMR spectra of CD-BZ, TPE-FFC—CMP, and Py-FFC—CMP individually and of their corresponding ICs. The spectra of their ICs feature signals for both CD-BZ and the FFC—CMPs, again implying that both components were present in the ICs. The signals of the glucose units in the spectrum of the pure CD-BZ were resolved [Fig. 2(a)], whereas in the spectra of the ICs they were unresolved [Fig. 2(c) and 2(e)], suggesting the formation of a symmetrical cyclic conformation for the CD in the ICs, with each glucose unit experiencing a similar chemical environment. Fig. 5 displays the XRD patterns of CD-BZ, TPE-FFC—CMP, and Py-FFC CMP individually and of their corresponding ICs. The XRD pattern of the pure CD-BZ revealed a crystalline structure, with peaks at 12.4, 18.4, and 24.4°[70]. The peaks for CD-BZ were broader than those of pure β-CD, suggesting that the crystalline structure was slightly distorted

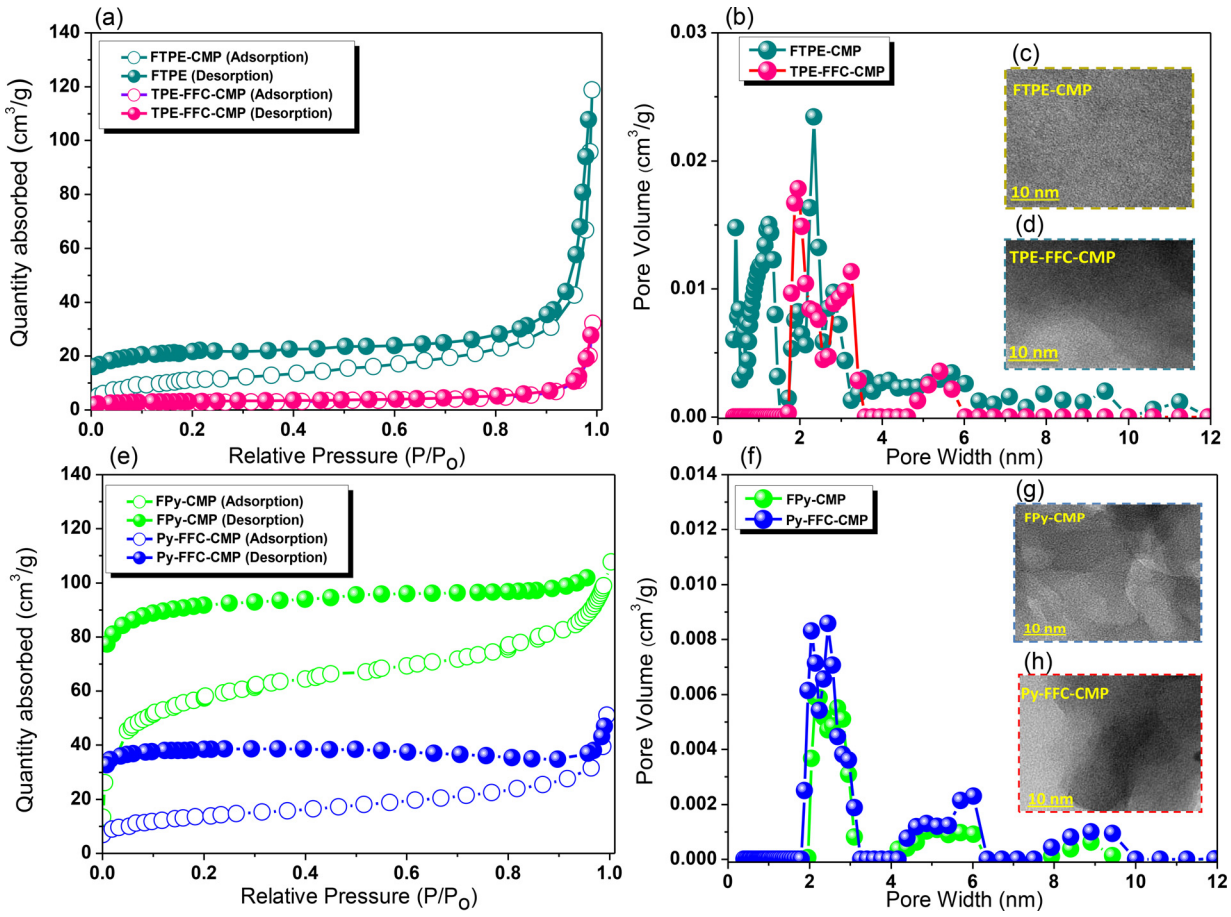

Fig. 3. (a, e) N_2 adsorption/desorption isotherms of (a) FTPE-CMP and TPE-FFC—CMP and (e) FPy-CMP and Py-FFC—CMP. (b, f) Pore size distribution curves of (b) FTPE-CMP and TPE-FFC—CMP and (f) FPy-CMP and Py-FFC—CMP. (c, d, g, h) TEM images of (c) FTPE-CMP, (d) TPE-FFC—CMP, (g) FPy-CMP, and (h) Py-FFC—CMP.

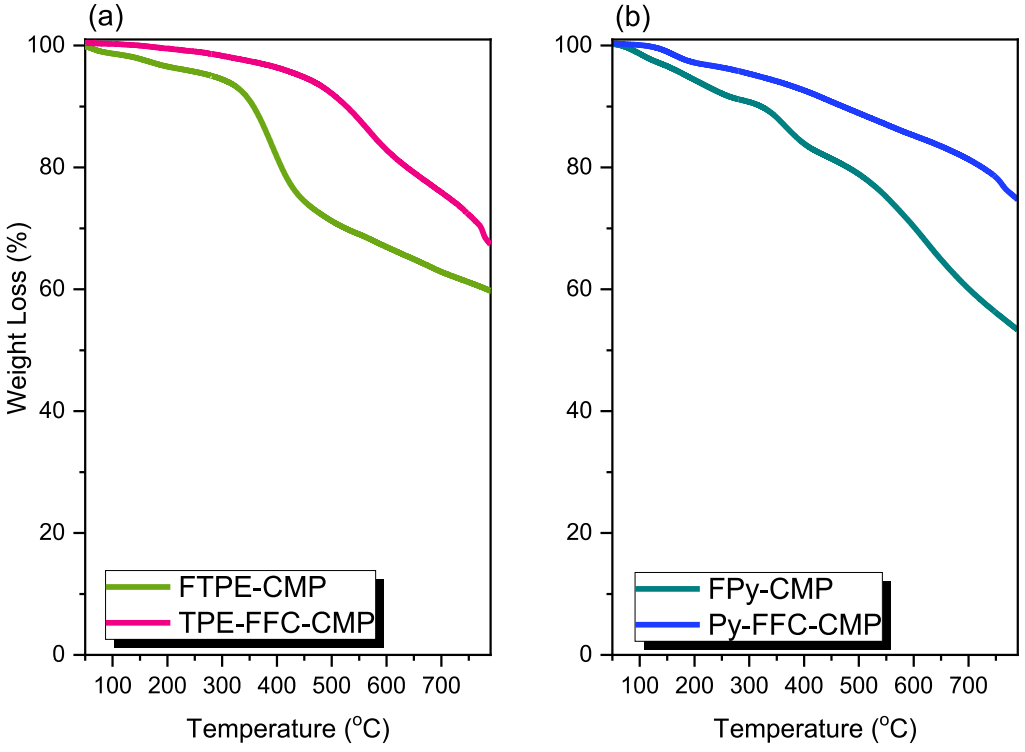

Fig. 4. TGA traces of (a) FTPE-CMP and TPE-FFC—CMP and (b) FPy-CMP and Py-FFC—CMP.

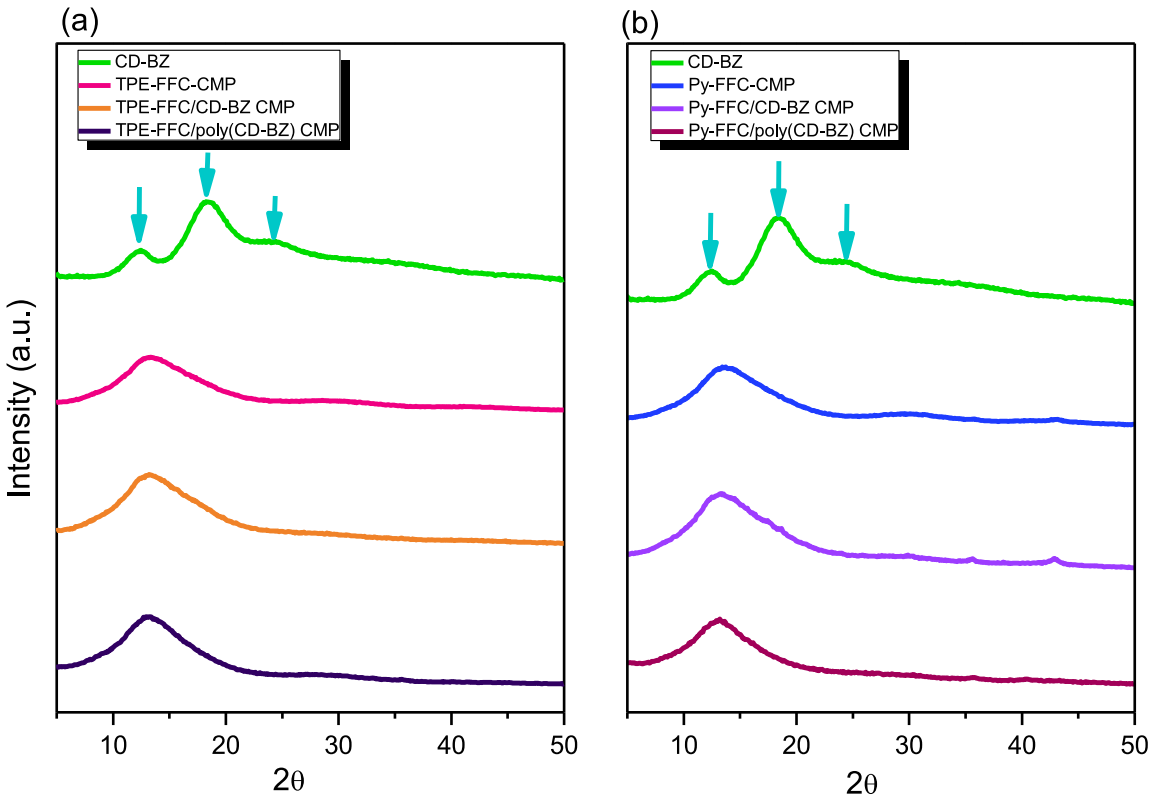

Fig. 5. XRD patterns of (a) CD-BZ, TPE-FFC—CMP, TPE-FFC/CD-BZ CMP, and TPE-FFC/Poly(CD-BZ) CMP and (b) CD-BZ, Py-FFC—CMP, Py-FFC/CD-BZ CMP, and Py-FFC/Poly(CD-BZ) CMP.

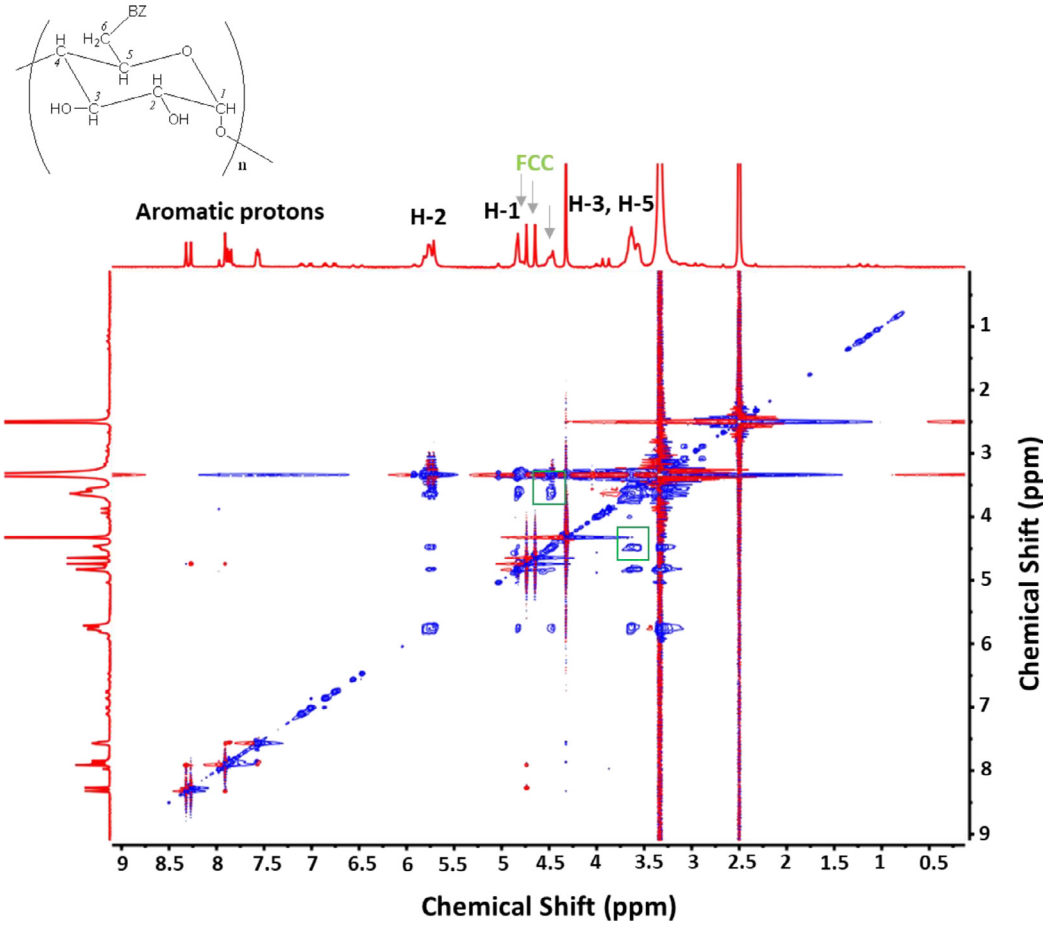

Fig. 6. 2D NOESY ^{1}H NMR spectra of FFC—CMP/CD-BZ (β-CD:FFC, 1:1) in DMSO-d_6.

Table 1
BET and TGA data for the CMPs prepared in this study.

Sample	Surface area (m^2/g)	Pore size (nm)	T_{d10} (°C)	Char Yield (%)
FTPE-CMP	31	1.24–2.37	357	59.6
TPE-FFC—CMP	8	0.47–2.83	527	67.3
FPy-CMP	191	2.14–5.85	321	53.2
Py-FFC—CMP	50	1.96–5.48	470	74.7

as a result of one of the OH groups being substituted by a BZ unit. In contrast to the pattern of the pure CD-BZ, those of both FFC—CMP/CD-BZ ICs featured amorphous halos, consistent with CD-BZ having formed ICs with the FFC units of the CMP frameworks, as displayed in Schemes 1(c) and 1(d); the CD-BZ units were isolated and, therefore, both FFC—CMP/CD-BZ ICs possessed amorphous structures.

The FFC/CD-BZ and both FFC—CMP/CD-BZ ICs were also thermally stable, based on TGA analyses (Fig. 7). The FFC/CD-BZ IC provided a value of T_{d10} of 315 °C and a char yield of 27.6 wt% at 800 °C; these values were, as expected, between those of the pure CD-BZ (T_{d10} = 236 °C; char yield = 7.4 wt%) and pure FFC (T_{d10} = 347 °C; char yield = 31.3 wt%) [Fig. 7(a)]. We observed similar phenomena for the TPE-FFC—CMP/CD-BZ IC [T_{d10} = 311 °C; char yield = 47.2 wt%; Fig. 7 (b)] and the Py-FFC—CMP/CD-BZ IC [T_{d10} = 322 °C; char yield = 61.1 wt%; Fig. 7(c)], with values again being between those of the pure CD-BZ and the corresponding FFC—CMPs. Furthermore, the TGA traces of all of the ICs revealed three-step thermal degradation: water desorption in the first step (ca. 3 wt% loss) at 100–200 °C, the FFC derivatives decomposing primarily in the second step at 200–400 °C, and CD-BZ and the remaining FFC decomposing mainly in the final step at temperatures above 400 °C. All of the characterization data obtained through these FTIR spectroscopic, solid-state NMR spectroscopic, XRD, and TGA analyses were consistent with the formation of FFC—CMP/CD-BZ ICs.

The FFC—CMP/CD-BZ ICs reported herein are the first examples of CMP materials possessing BZ units assembled through host–guest interactions of FFC and β-CD units. Most interestingly, the BZ units of these FFC—CMP/CD-BZ ICs could undergo ROP, readily converting to phenolic and tertiary amino functional groups through one-step chemical transformations in the solid state [Schemes 1(e) and 1(f)]; this process has never been reported previously for CMPs featuring host–guest interactions with an acceptable surface area and pore volume. To investigate the ROP behavior of the FFC—CMP/CD-BZ ICs in the solid state, we recorded their XRD patterns (Fig. 5); the XRD patterns of the FFC—CMP/poly(CD-BZ) ICs were both similar to those of the uncured FFC—CMP/CD-BZ ICs, indicating that no morphological change had occurred during their ROPs. Furthermore, Fig. 8 displays the FTIR spectra and TGA traces of the FFC—CMP/CD-BZ ICs before and after ROP. Fig. 8(a) and 8(b) reveals that the peaks at 937 and 1157 cm^{-1} for the oxazine ring and C–O–C stretching, respectively, both disappeared after thermal curing polymerization of both FFC—CMP/CD-BZ ICs. All of the signals become broad after the thermal ROPs, consistent with cross-linked network structures that restricted the molecular vibrations of both FFC—CMP/poly(CD-BZ) ICs. We also investigated the thermal stabilities of the FFC—CMP/CD-

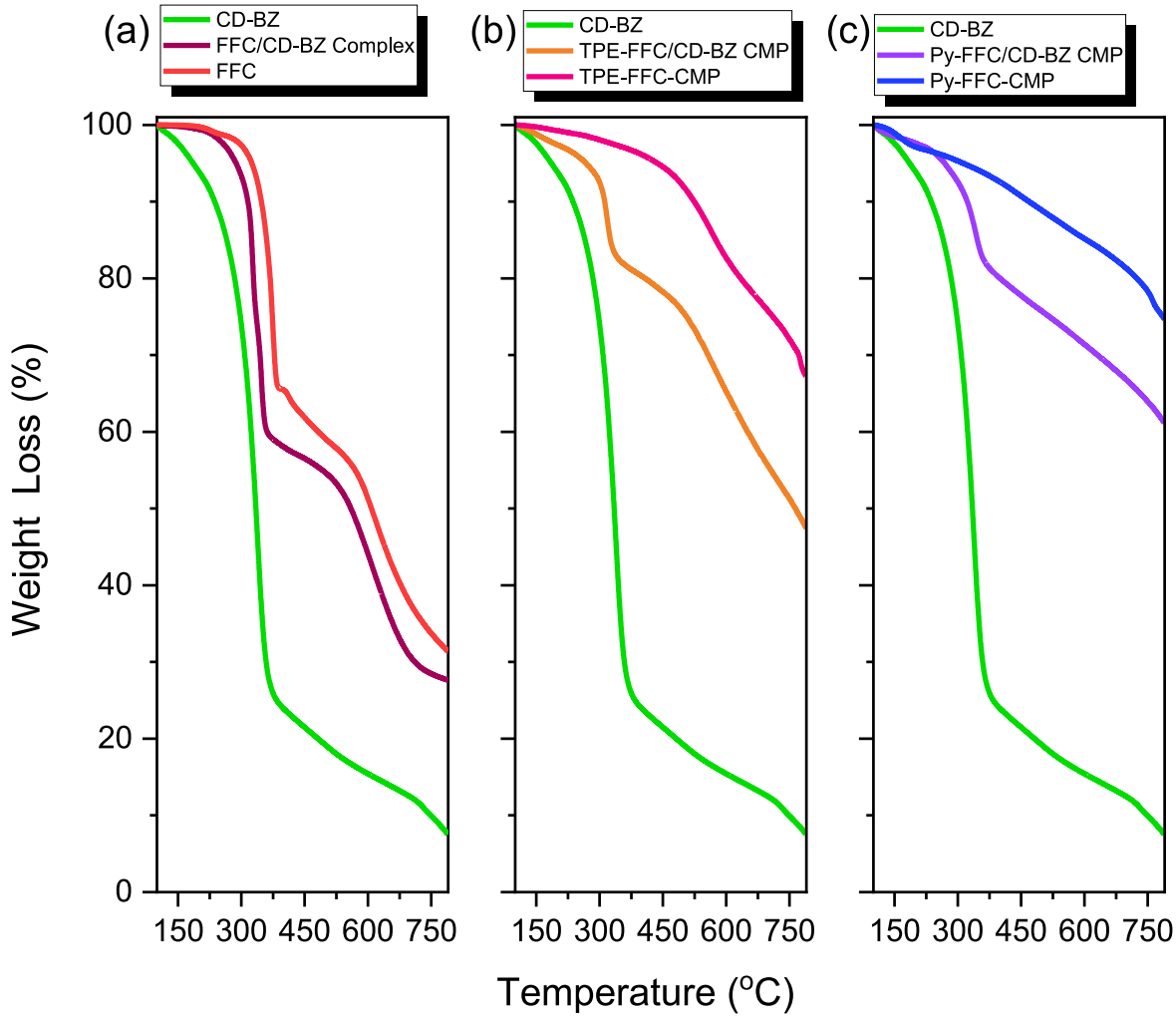

Fig. 7. TGA traces of (a) CD-BZ, FFC, and the FFC/CD-BZ complex; (b) CD-BZ, TPE-FFC—CMP, and the TPE-FFC/CD-BZ CMP; and (c) CD-BZ, Py-FFC—CMP, and the Py-FFC/CD-BZ CMP.

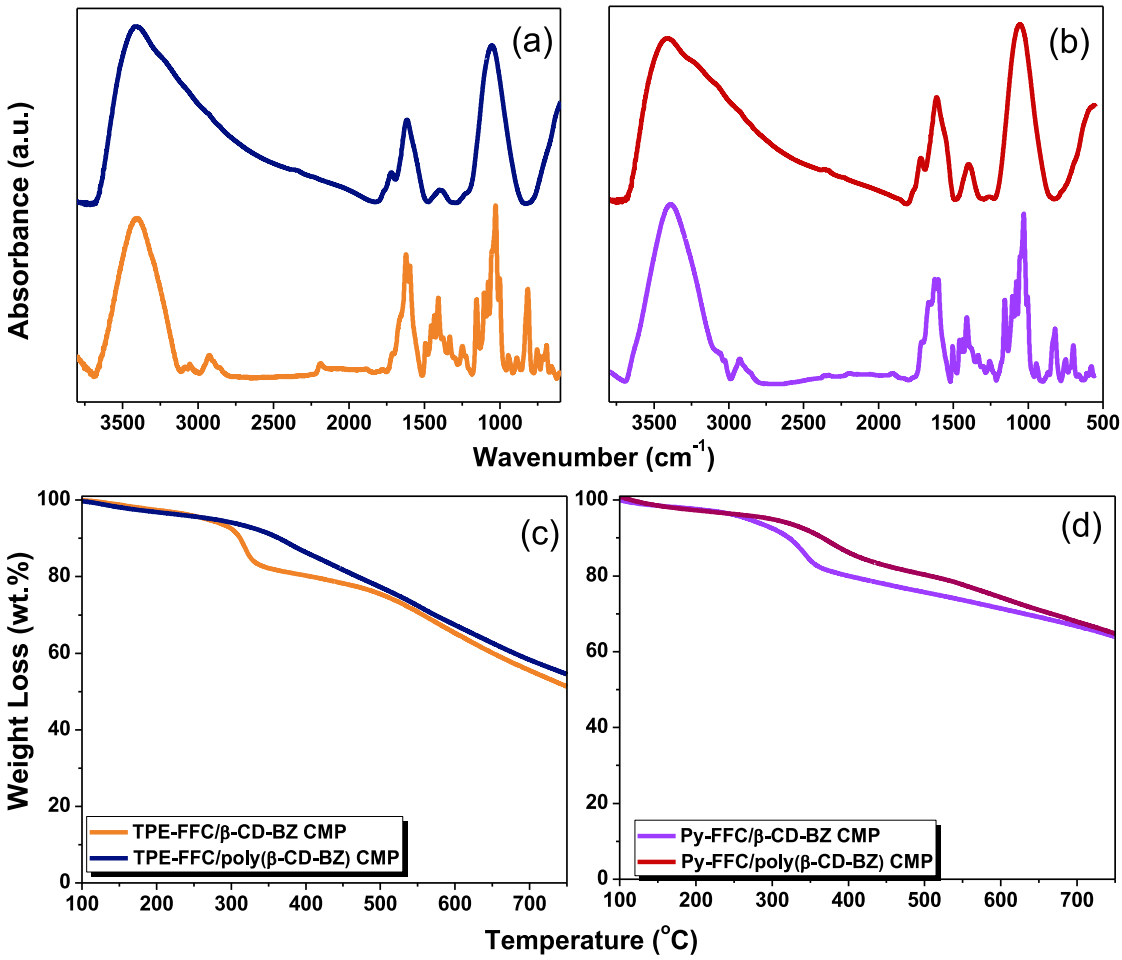

Fig. 8. (a, b) FTIR spectra of (a) TPE-FFC/CD-BZ CMP and TPE-FFC/Poly(CD-BZ) CMP and (b) Py-FFC/CD-BZ CMP and Py-FFC/Poly(CD-BZ) CMP. (c, d) TGA traces of (c) TPE-FFC/CD-BZ CMP and TPE-FFC/Poly(CD-BZ) CMP and (d) Py-FFC/CD-BZ CMP and Py-FFC/Poly(CD-BZ) CMP.

BZ ICs before and after their thermal ROPs [Fig. 8(c) and 8(d); Table S1]. After thermal ROP of the TPE-FFC/poly(CD-BZ) CMP IC, the value of T_{d10} (364 °C) and the char yield (50.1 wt%) were both higher than those prior to the thermal ROP (T_{d10} = 311 °C; char yield = 47.2 wt%); similarly, the Py-FFC/poly(CD-BZ) CMP IC also exhibited a higher value of T_{d10} (366 °C) and a higher char yield (62.1 wt%) after its thermal ROP (prior to ROP: T_{d10} = 322 °C; char yield = 61.1 wt%). Thus, both of the FFC—CMP/poly(CD-BZ) ICs had outstanding thermal decomposition temperatures, presumably due to their greater number of intramolecular (OH···N) and intermolecular (OH···O) hydrogen bonds after their ROPs. In addition, the thermal stabilities of these two FFC—CMP/poly(CD-BZ) ICs were also higher than those of FTPE-CMP (T_{d10} = 357 °C) and FPy-CMP (T_{d10} = 321 °C), in the absence of the FFC/poly(CD-BZ) IC units; thus, the thermal curing of the CD-BZ units did, indeed, improve the thermal stability.

3.4. CO_2 uptake

In addition to developing a new approach for the solid-state chemical transformations of CMPs, through the application of host–guest interactions of FFC and β-CD units and subsequent ROPs of their BZ units, we suspected that the new functionality in the CMPs—the cavities and glucose units of the β-CD moieties and the phenolic OH units and Mannich bridges of the BZ moieties—might be capable of interacting with molecules of CO_2. Fig. 9 and Table S1 summarize the CO_2 capture, recorded at 298 °C and 1 bar, of FFC—CMP and the FFC—CMP/CD-BZ ICs before and after their ROPs. Fig. 9(a) reveals that the CO_2 uptake abilities of TPE-FFC—CMP and the TPE-FFC—CMP/CD-BZ and TPE-FFC—CMP/poly (CD-BZ) ICs were 1.17, 0.81, and 1.31 mmol g^{-1}, respectively; Fig. 9 (b) reveals that for Py-FFC—CMP and the Py-FFC—CMP/CD-BZ and Py-FFC—CMP/poly(CD-BZ) ICs these values were 1.89, 1.04, and 1.42 mmol g^{-1}, respectively. The CO_2 capture ability of Py-FFC—CMP was higher than that of TPE-FFC—CMP because the former had a higher pore volume and surface area—generally favorable for CO_2 uptake in a porous material lacking polar functional groups. The CO_2 capture ability decreased for both FFC—CMP/CD-BZ ICs, presumably because the attached CD-BZ units decreased the surface area and pore volume. The CO_2 capture abilities of the FFC—CMP/poly(CD-BZ) ICs after their ROPs were, however, higher than those of their corresponding FFC—CMP/CD-BZ ICs, presumably because the high abundance of N atoms and phenolic OH groups derived from the BZ units were capable of acid/base (N···C=O), hydrogen bonding (OH···O=C), or other high-affinity interactions with CO_2 [48]. Interestingly, the CO_2 uptake of the TPE-FFC—CMP/poly(CD-BZ) IC after ROP (1.31 mmol g^{-1}) was higher than that of TPE-FFC—CMP (1.17 mmol g^{-1}), but lower than that of the Py-FFC—CMP/poly(CD-BZ) IC (1.42 mmol g^{-1}) after ROP, which itself was lower than that of Py-FFC—CMP which might be attributed to degrade some functional groups during the curing process and low N atoms contents inside Py-FFC—CMP/poly(CD-BZ) IC. As a result, the overall CO_2 capture abilities of our CMP materials were strongly correlated to their pore volumes, the surface chemical functional groups, and surface areas.

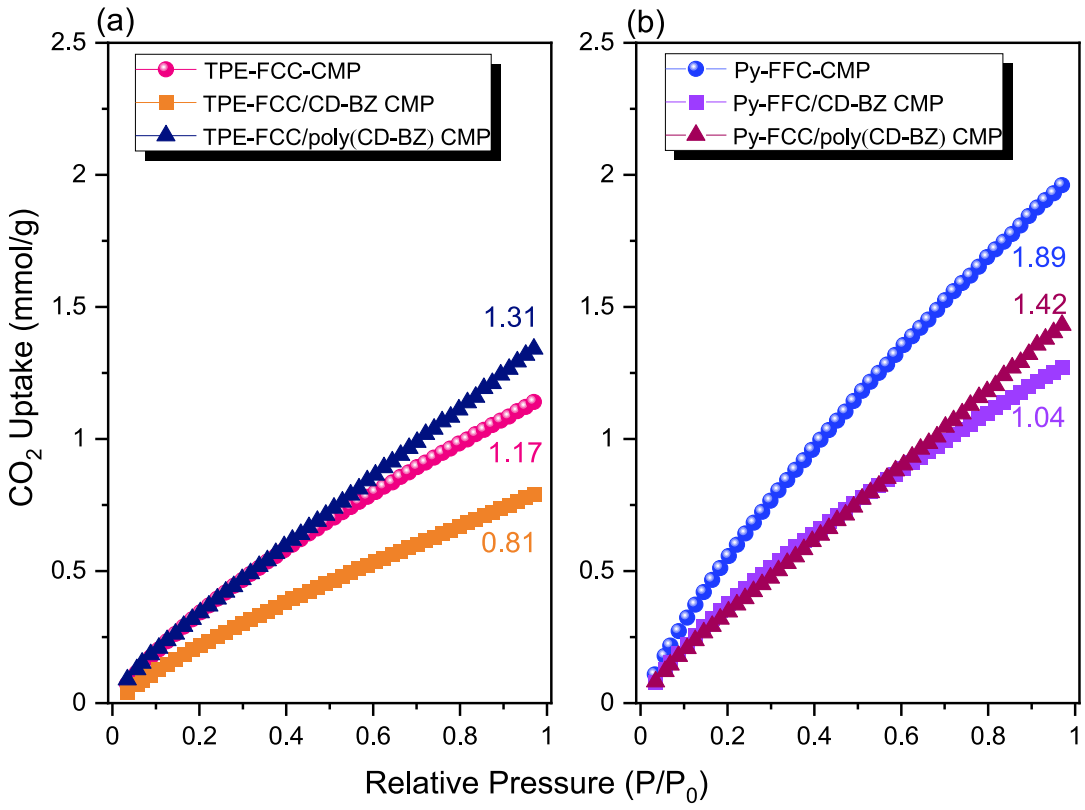

Fig. 9. CO_2 capture of (a) TPE-FFC—CMP, TPE-FFC/CD-BZ CMP, and TPE-FFC/Poly(CD-BZ) CMP and (b) Py-FFC—CMP, Py-FFC/CD-BZ CMP, and Py-FFC/Poly(CD-BZ) CMP.

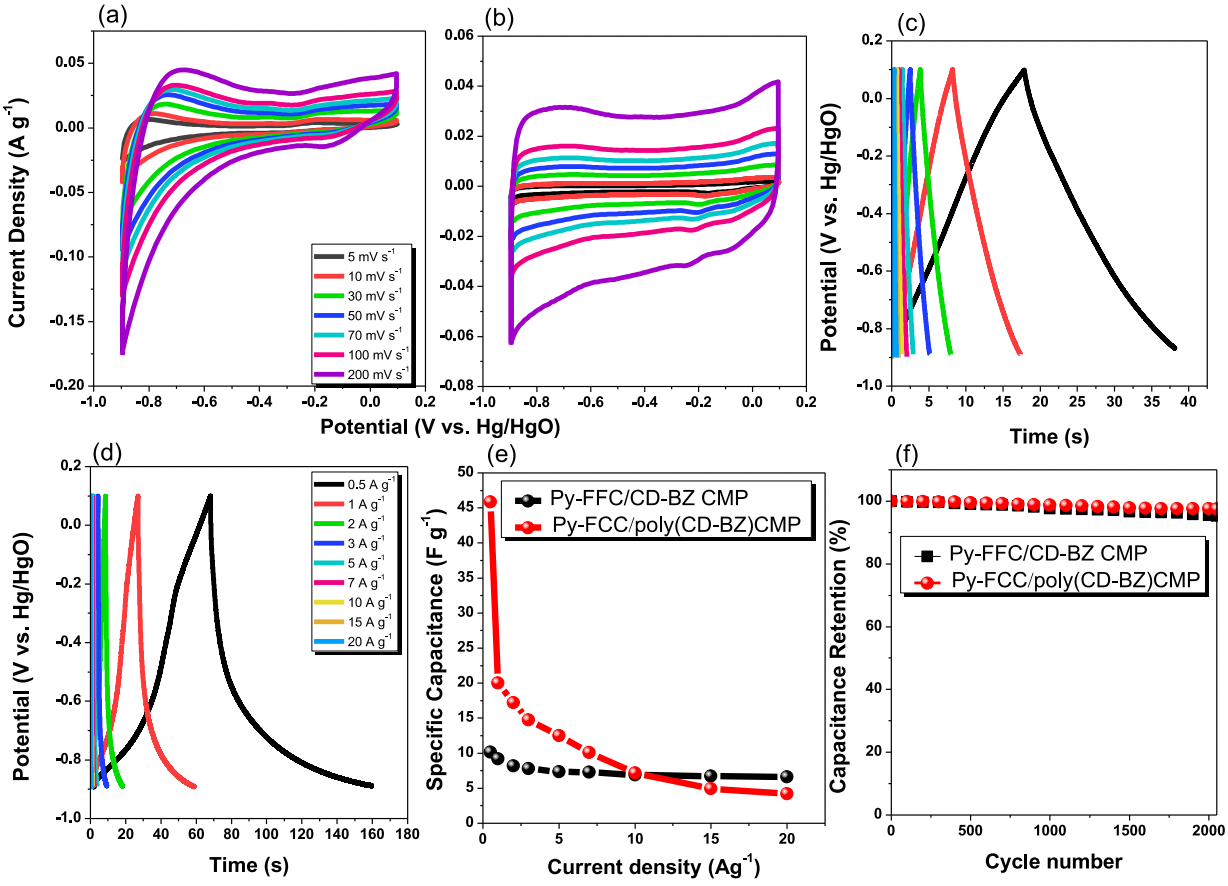

Fig. 10. (a, b) CV curves of (a) Py-FFC/CD-BZ CMP and (b) Py-FFC/Poly(CD-BZ) CMP. (c, d) GCD curves of (c) Py-FFC/CD-BZ CMP and (d) Py-FFC/Poly(CD-BZ) CMP, measured at various current densities. (e) Specific capacitances of Py-FFC/CD-BZ CMP and Py-FFC/Poly(CD-BZ) CMP, measured at current densities from 0.5 to 20 A g^{-1}. (f) Cycling stabilities of Py-FFC/CD-BZ CMP and Py-FFC/Poly(CD-BZ) CMP, measured at 10 A g^{-1} over 2000 cycles.

3.5. Electrochemical performance

We measured the electrochemical performance of our CMP materials in terms of their galvanostatic charge/discharge (GCD) and CV behavior, in 1 M aqueous KOH using a three-electrode system. Figures S6(a) and S6(b) display the CV curves of TPE-FFC—CMP and Py-FFC—CMP, respectively, recorded in the potential window from +0.1 to −0.90 V (vs. Hg/HgO) at various sweep rates from 5 to 200 mV s^{-1}. The CV curves of these two FFC—CMP samples had rectangular shapes featuring humps, indicating that their capacitive responses originated from both electric double-layer capacitance (EDLC) and pseudocapacitance, arising from the presence of electron-rich phenyl rings and electroactive ferrocene backbones, in which redox processes occurred during the charging and discharging processes [71,75-79]. The ferrocene backbones within TPE-FFC—CMP and Py-FFC—CMP underwent reversible one-electron redox processes, as revealed in the voltammetric profiles [Figures S6(a) and S6(b)]. The current density provided by Py-FFC—CMP was higher than that of TPE-FFC—CMP. The peak current densities increased upon increasing the sweep rate from 5 to 200 mV s^{-1}, while the shapes of the CV curves were retained, indicative of good electron transporting properties and facile kinetics [9,80,81]. Figures S6(c) and S6(d) present the GCD curves of TPE-FFC—CMP and Py-FFC—CMP, respectively, measured at various current densities from 0.5 to 20 A g^{-1}. The GCD curves of these two FFC—CMP samples were triangular with a slight bend, suggesting both EDLC and pseudocapacitive characteristics [82–84]. The GCD curves of these two samples displayed the typical features of pseudocapacitors, with high symmetry indicating good electrochemical reversibility and capacitance performance [85]. The discharging time of Py-FFC—CMP was longer than that of TPE-FFC—CMP [Figures S6(c) and S6(d)], indicating that the capacitance of the former was greater than that of the latter [Figure S6(e)]. Figure S6(e) presents the specific capacitances of TPE-FFC—CMP and Py-FFC—CMP, calculated from GCD curves using Eq. (S1). The capacitance of Py-FFC—CMP was relatively higher (5.07 F g^{-1}) than that of TPE-FFC—CMP (4.8 F g^{-1}) at a current density of 0.5 A g^{-1}, presumably because Py-FFC—CMP featured a higher surface area (50 m^2 g^{-1}), higher pore volume (0.07 cm^3 g^{-1}), better π-stacking, and a more ordered structure. We tested the durability of these two samples by cycling them over 2000 times at 10 A g^{-1} [Figure S6(f)]. TPE-FFC—CMP and Py-FFC—CMP both displayed good cycling stability [Figure S6(f)], with retentions of their original capacitances of 89.87% and 90.65%, respectively, after 2000 cycles. Figures S7(a) and S7(b) present the CV profiles of the TPE-FFC—CMP/CD-BZ and TPE-FFC—CMP/poly(CD-BZ) ICs, respectively. Their CV curves were rectangular, indicating that their capacitive responses originated mainly from EDLC (with minor pseudocapacitance), arising from the presence of electron-rich phenyl rings, electroactive ferrocene backbones, and heteroatoms (N and O atoms) [75–79]. In addition, the current density of the TPE-FFC—CMP/poly(CD-BZ) IC after ROP was higher than that of the TPE-FFC—CMP/CD-BZ IC. Figures S7(c) and S7(d) present the GCD curves of the TPE-FFC—CMP/CD-BZ and TPE-FFC—CMP/poly(CD-BZ) ICs, respectively. These GCD curves were triangular with a slight bend, suggesting the characteristics of both EDLC and pseudocapacity [78–81]. The discharging time of the TPE-FFC—CMP/poly(CD-BZ) IC was longer than that of the TPE-FFC—CMP/CD-BZ IC [Figures S7(c) and S7(d)], indicating that the capacitance of the former was greater than that of the latter [Figure S7(e)]. Figure S7(e) presents the specific capacitances of the TPE-FFC—CMP/CD-BZ and TPE-FFC—CMP/poly(CD-BZ) ICs. The capacitance of the TPE-FFC—CMP/poly(CD-BZ) IC after ROP (37.07 F g^{-1}) was much higher than that of the TPE-FFC—CMP/CD-BZ IC (7.53 F g^{-1}) at a current density of 0.5 A g^{-1}. We attribute this behavior to the high contents of N atoms and phenolic OH groups derived from the BZ units. These two TPE-FFC—CMP/CD-BZ and TPE-FFC—CMP/poly(CD-BZ) ICs displayed excellent cycling stability [Figure S7(f)], with retentions of their original capacitances of 94.3 and 96.03%, respectively, after 2000 cycles. Fig. 10(a) and 10(b) displays the CV curves of the Py-FFC—CMP/CD-BZ and Py-FFC—CMP/poly(CD-BZ) ICs, respectively. These curves were rectangular, indicating that the capacitive responses originated mainly from EDLC (with minor pseudocapacitance), arising from the presence of electron-rich phenyl rings, electroactive ferrocene backbones, and heteroatoms (N and O atoms) [75–79]. In addition, the current density of the Py-FFC—CMP/poly(CD-BZ) IC after ROP was higher than that of the Py-FFC—CMP/CD-BZ IC. Fig. 10(c) and 10(d) presents the GCD curves of the Py-FFC—CMP/CD-BZ and Py-FFC—CMP/poly(CD-BZ) ICs, respectively. These GCD curves were triangular shapes with a slight bend, suggesting the characteristics of both EDLC and pseudocapacity [79–81]. The discharging time of the Py-FFC—CMP/poly(CD-BZ) IC after ROP was longer than that of the Py-FFC—CMP/CD-BZ IC [Fig. 10(c) and 10(d)], indicating that the capacitance of the former was larger than that of the latter [Fig. 10(e)]. Fig. 10(e) provides the specific capacitances of the Py-FFC—CMP/CD-BZ and Py-FFC—CMP/poly(CD-BZ) ICs. The capacitance of the Py-FFC—CMP/poly(CD-BZ) IC after ROP (46 F g^{-1}) was much higher than that of the Py-FFC—CMP/CD-BZ IC (10.15 F g^{-1}) at a current density of 0.5 A g^{-1}, presumably because of the high contents of N atoms and phenolic OH groups derived from the BZ units. These two Py-FFC—CMP/CD-BZ and Py-FFC—CMP/poly(CD-BZ) ICs displayed excellent cycling stability [Fig. 10(f)], with retentions of their original capacitances of 95.2% and 97.49%, respectively, after 2000 cycles. Table S2 compares the specific capacitances of these materials with those reported previously for other materials. Gratifyingly, the specific capacitance of the Py-FFC—CMP/poly(CD-BZ) IC after ROP was higher than those of previously reported covalent organic frameworks (COFs) and other CMPs [82,86-89].

4. Conclusions

Two FFC—CMP/CD-BZ CMP inclusion complexes were formed through supramolecular host-guest interactions between the benzoxazine-linked Cyclodextrin (CD-BZ) and ferrocene unit of FFC—CMP. The obtained FFC—CMP/CD-BZ ICs were examined by using FTIR, 2D NOESY ^{1}H NMR, solid-state ^{13}C CP/MAS NMR, X-ray diffraction, and TGA analyses. After thermal curing polymerization (ROP), the Py-FFC/poly(CD-BZ) CMP ICs exhibited outstanding thermal stability (T_{d10} = 366 °C) with char yield of 62.1%, which could be attributed to the presence of intramolecular (OH—N) and intermolecular (OH—O) hydrogen bonding interactions. Interestingly, the Py-FFC—CMP/poly(CD-BZ) ICs revealed higher CO_2 uptake ability of 1.42 mmol $g^{-1}$and higher specific capacitance of 46 F g^{-1}at current density 0.5 A g^{-1}. In addition, we expect that these new porous materials could be used for other potential applications such as dyes adsorption, iodine capture, and photocatalytic H_2 evolution from water.

Declaration of Competing Interest

The authors declare that they have no known competing financial interests or personal relationships that could have appeared to influence the work reported in this paper.

Acknowledgments

This study was supported financially by the Ministry of Science and Technology, Taiwan, under contracts MOST 108-2638-E-002-003-MY2, and 108-2221-E-110-014-MY3. The authors thank to the staff at National Sun Yat-sen University for assistance with TEM (ID: EM022600) experiments.

Supplementary materials

Supplementary material associated with this article can be found in the online version at doi:10.1016/j.jtice.2021.10.010.

References

[1] Samy MM, Mohamed MG, EL-Mahdy AFM, Mansoure TH, Wu KCW, Kuo SW. High-performance supercapacitor electrodes prepared from dispersions of tetrabenzonaphthalene-based conjugated microporous polymers and carbon nanotubes. ACS Appl Mater Interfaces 2021. doi: 10.1021/acsami.1c05720.

[2] Zhang WJ, Tang JT, Yu W, Huang Q, Fu Y, Kuang GC, Pan CY, Yu GP. Visible light-driven C-3 functionalization of indoles over conjugated microporous polymers. ACS Catal 2018;8:8084–91.

[3] EL-Mahdy AFM, Elewa AM, Huang SW, Chou HH. Dual-function fluorescent covalent organic frameworks: HCl sensing and photocatalytic H_2 evolution from water. Adv Optical Mater 2020;8:2000641.

[4] Zhang C, He Y, Mu P, Wang X, He Q, Chen Y, Zeng J, Wang F, Xu Y, Jiang JX. Toward high performance thiophene containing conjugated microporous polymer anodes for lithium-ion batteries through structure design. Adv Funct Mater 2018;28:1705432.

[5] Wu JY, Mohamed MG, Kuo SW. Directly synthesized nitrogen-doped microporous carbons from polybenzoxazine resins for carbon dioxide capture. Polym Chem 2017;8:5481–9.

[6] Kou Y, Xu Y, Guo Z, Jiang D. Supercapacitive energy storage and electric power supply using an Aza-fused π-conjugated microporous framework. Angew Chem Int Ed 2011;50:8753–7.

[7] Li JG, Lee PY, Ahmed MMM, Mohamed MG, Kuo SW. Varying the hydrogen bonding strength in phenolic/PEO-b-PLA blends provides mesoporous carbons having large accessible pores suitable for energy storage. Macromol Chem Phys 2020;221:2000040.

[8] Zhu J, Yang C, Lu C, Zhang F, Yuan Z, Zhuang X. Two dimensional porous polymers: from sandwich-like structure to layered skeleton. Acc Chem Res 2018;51 3191-02.

[9] EL-Mahdy AFM, Mohamed MG, Mansoure TH, Yu HH, Chen T, Kuo SW. Ultrastable tetraphenyl-p-phenylenediamine based covalent organic frameworks as platforms for high-performance electrochemical supercapacitors. Chem Commun 2019;55:14890–3.

[10] Aly KI, Sayed MM, Mohamed MG, Kuo SW, Younis O. A facile synthetic route and dual function of network luminescent porous polyester and copolyester containing porphyrin moiety for metal ions sensor and dyes adsorption. Microporous Mesoporous Mater 2020;298:110063.

[11] Mohamed MG, Mahmoud MMA, Wei TD, Kuo SW. Meso/microporous carbons from conjugated hyper-crosslinked polymers based on tetraphenylethene for high-performance CO_2 capture and supercapacitor. Molecules 2021;26:738.

[12] Wang B, Xie Z, Li Y, Yang Z, Chen L. Dual-functional conjugated nanoporous polymers for efficient organic pollutants treatment in water: a synergistic strategy of adsorption and photocatalysis. Macromolecules 2018;51:3443–9.

[13] Abuzeid HR, EL-Mahdy AFM, Kuo SW. Covalent organic frameworks: design principles, synthetic strategies, and diverse applications. Giant 2021;6:1000054.

[14] Mohamed MG, Atayde EC, Matsagar BM, Na J, Yamauchi Y, Wu KCW, Kuo SW. Construction hierarchically mesoporous/microporous materials based on block copolymer and covalent organic framework. J Taiwan Inst Chem Eng 2020;112:180–92.

[15] Zhang T, Xing G, Chen W, Chen L. Porous organic polymers: a promising platform for efficient photocatalysis. Mater Chem Front 2020;4:332–53.

[16] Mohamed MG, Lee CC, EL-Mahdy AFM, Luder J, Yu MH, Li Z, Zhu Z, Chueh CC, Kuo SW. Exploitation of Two dimensional conjugated covalent organic frameworks based on tetraphenylethylene with bicarbazole and pyrene units and applications in perovskite solar cells. J Mater Chem A 2020;8:11448–59.

[17] Vyas VS, Haase F, Stegbauer L, Savasci G, Podjaski F, Ochsenfeld C, Lotsch BV. A tunable azine covalent organic framework platform for visible light-induced hydrogen generation. Nat Commun 2015;6:8508–16.

[18] Mohamed MG, Liu NY, EL-Mahdy AFM, Kuo SW. Ultrastable luminescent hybrid microporous polymers based on polyhedral oligomeric silsesquioxane for CO_2 uptake and metal ion sensing. Microporous Mesoporous Mater 2021;311:110695.

[19] Schmidt J, Werner M, Thomas A. Conjugated microporous polymer networks via yamamoto polymerization. Macromolecules 2009;42:4426–9.

[20] Liu QQ, Tang Z, Wu MD, Liao B, Zhou H, Ou BL, Yu GP, Zhou ZH, Li XJ. Novel ferrocene-based nanoporous organic polymers for clean energy application. RSC Adv 2015;5:8933–77.

[21] Fischer S, Schimanowitz A, Dawson R, Senkovska I, Kaskel S, Thomas A. Cationic microporous polymer networks by polymerisation of weakly coordinating cations with CO_2-storage ability. J Mater Chem A 2014;2:11825–9.

[22] Schmidt J, Weber J, Epping JD, Antonietti M, Thomas A. Microporous conjugated poly(thienylene arylene) networks. Adv Mater 2009;21:702–5.

[23] Wang H, Cheng Z, Liao Y, Li J, Weber J, Thomas A, Faul CFJ. Conjugated microporous polycarbazole networks as precursors for nitrogen-enriched microporous carbons for CO_2 storage and electrochemical capacitors. Chem. Mater 2017;29:4885–93.

[24] Wang Z, Yuan S, Mason A, Reprogle B, Liu DJ, Yu L. Nanoporous porphyrin polymers for gas storage and separation. Macromolecules 2012;45:7413–9.

[25] Jiang JX, Su FB, Trewin A, Wood CD, Niu HJ, Jones JTA, Khimyak YZ, Cooper AI. Synthetic control of the pore dimension and surface area in conjugated microporous polymer and copolymer networks. J Am Chem Soc 2008;130:7710–20.

[26] Vilela F, Zhang K, Antonietti M. Conjugated porous polymers for energy applications. Energy Environ Sci 2012;5:7819–32.

[27] Xu Y, Nagai A, Jiang D. Core-shell conjugated microporous polymers: a new strategy for exploring color-tunable and -controllable light emissions. Chem Commun 2013;49:1591–3.

[28] Waller PJ, Lyle SJ, Popp TO, Diercks CS, Reimer JA, Yaghi OM. Chemical conversion of linkages in covalent organic frameworks. J Am Chem Soc 2016;138:15519–22.

[29] Haase F, Troschke E, Savasci G, Banerjee T, Duppel V, Dorfler S, Grundei MMJ, Ochsenfeld C, Kaskel S, Lotsch BV. Topochemical conversion of an imine- into A thiazole-linked covalent organic framework enabling real structure analysis. Nat Commun 2018;9:2600.

[30] Liu H, Chu J, Yin Z, Cai X, Zhuang L, Deng H. Covalent organic frameworks linked by amine bonding for concerted electrochemical reduction of CO_2. Chem 2018;4:1696–709.

[31] Li X, Zhang C, Cai S, Lei X, Altoe V, Hong F, Urban JJ, Ciston J, Chan EM, Liu Y. Facile transformation of imine covalent organic frameworks into ultrastable crystalline porous aromatic frameworks. Nat Commun 2018;9:2998.

[32] Waller PJ, Alfaraj YS, Diercks CS, Jarenwattananon NN, Yaghi OM. Conversion of imine to oxazole and thiazole linkages in covalent organic frameworks. J Am Chem Soc 2018;140:9099–103.

[33] Wei PF, Qi MZ, Wang ZP, Ding SY, Yu W, Liu Q, Wang LK, Wang HZ, An WK, Wang W. Benzoxazole-linked ultrastable covalent organic frameworks for photocatalysis. J Am Chem Soc 2018;140:4623–31.

[34] Stewart D, Antypov D, Dyer MS, Pitcher MJ, Katsoulidis AP, Chater PA, Blanc F, Rosseinsky MJ. Stable and ordered amide frameworks synthesised under reversible conditions which facilitate error checking. Nat Commun 2017;8:1102.

[35] Zhao C, Lyu H, Ji Z, Zhu C, Yaghi OM. Ester-linked crystalline covalent organic frameworks. J Am Chem Soc 2020;142:14450–4.

[36] Hasse F, Hirschle P, Freund R, Furukawa S, Ji ZS, Wuttke S. Beyond frameworks: structuring reticular materials across nano-, meso-, and bulk regimes. Angew Chem Int Ed 2020;59:22350–70.

[37] Lyle SJ, Popp TOS, Waller PJ, Pei X, Reimer JA, Yaghi OM. Multistep solid-state organic synthesis of carbamate-linked covalent organic frameworks. J Am Chem Soc 2019;141:11253–8.

[38] Mohamed MG, Tsai MY, Su WC, EL-Mahdy AFM, Wang CF, Huang CF, Dai L, Chen T, Kuo SW. Nitrogen-doped microporous carbons derived from azobenzene and nitrile-functionalized polybenzoxazines for CO_2 uptake. Mater Today Commun 2020;24:101111.

[39] Zhang X, Mohamed MG, Xin Z, Kuo SW. A tetraphenylethylene-functionalized benzoxazine and copper(II) acetylacetonate form a high-performance polybenzoxazine. Polymer (Guildf) 2020;221:122552.

[40] Mohamed MG, Kuo SW. Functional silica and carbon nanocomposites based on polybenzoxazines. Macromol Chem Phys 2019;220:1800306.

[41] Mohamed MG, Mahdy A, Hegazy MA, Obaid RJ, Kuo SW, Aly KI. Synthesis and characterization of polybenzoxazine/clay hybrid nanocomposites for UV light shielding and anti-corrosion coatings on mild steel. J Polym Res 2021;28:297.

[42] Wang CF, Su YC, Kuo SW, Huang CF, Sheen YC, Chang FC. Low-surface-free-energy materials based on polybenzoxazines. Angew Chem Int Ed 2006;45:2248–51.

[43] Aly KI, Mohamed MG, Younis O, Mahross MH, Abdel-Hakim M, Sayed MM. Salicylaldehyde azine-functionalized polybenzoxazine: synthesis, characterization, and its nanocomposites as coatings for inhibiting the mild steel corrosion. Prog Org Coat 2020;138:105385.

[44] Mohamed MG, Kuo SW. Crown ether-functionalized polybenzoxazine for metal ion adsorption. Macromolecules 2020;53:2420–9.

[45] Mohamed MG, Ebrahium SM, Hammam AS, Kuo SW, Aly KI. Enhanced CO_2 capture in nitrogen-enriched microporous carbons derived from Polybenzoxazines containing azobenzene and carboxylic acid units. J Polym Res 2020;27:197.

[46] Mohamed MG, Kuo SW, Mahdy A, Ghayd IM, Aly KI. Bisbenzylidene cyclopentanone and cyclohexanone-functionalized polybenzoxazine nanocomposites: synthesis, characterization, and use for corrosion protection on mild steel. Mater Today Commun 2020;25:101418.

[47] Abuzeid HR, EL-Mahdy AFM, Ahmed MMM, Kuo SW. Triazine-functionalized covalent benzoxazine framework for direct synthesis of N-doped microporous carbon. Polym Chem 2019;10:6010–20.

[48] Mohamed MG, Chen TC, Kuo SW. Solid-state chemical transformations to enhance gas capture in benzoxazine-linked conjugated microporous polymers. Macromolecules 2021;54:5866–77.

[49] Yang LL, Tan XX;, Wang ZQ, Zhang X. Supramolecular polymers: historical development, preparation, characterization, and functions. Chem Rev 2015;115 7196−39.

[50] Wang F, Zhang J, Ding X, Dong S, Liu M, Zheng B, Li S, Wu L, Yu Y, Gibson HW, Huang F. Metal coordination mediated reversible conversion between linear and cross-linked supramolecular polymers. Angew Chem Int Ed 2010;49:1090–4.

[51] Whittell GR, Hager MD, Schubert US. Manners I Functional soft materials from metallopolymers and metallosupramolecular polymers. Nat Mater 2011;10:176–88.

[52] Aly KI, Mahdy A, Hegazy MA, Al-Muaikel NS, Kuo SW, Mohamed MG. Corrosion resistance of mild steel coated with phthalimide-functionalized polybenzoxazines. Coatings 2020;10:1114.

[53] Yu GC, Jie KC, Huang FH. Supramolecular amphiphiles based on host−guest molecular recognition motifs. Chem Rev 2015;115:7240–303.

[54] Xia DY, Wang P, Ji XF, Khashab NM, Sessler JL, Huang FH. Functional supramolecular polymeric networks: the marriage of covalent polymers and macrocycle-based host–guest interactions. Chem Rev 2020;120:6070–123.
[55] Xie Y, Wang X, Han X, Xue X, Ji W, Qi Z, Liu J, Zhao B, Ozaki Y. Sensing of polycyclic aromatic hydrocarbons with cyclodextrin inclusion complexes on silver nanoparticles by surface enhanced Raman scattering. Analyst 2010;135:1389–94.
[56] Giulbudagian M, Hönzke S, Bergueiro J, Işık D, Schumacher F, Saeidpour S, Lohan SB, Meinke MC, Teutloff C, Schäfer-Korting M, Yealland G, Kleuser B, Hedtrichb S, Calderón M. Enhanced topical delivery of dexamethasone by β-cyclodextrin decorated thermoresponsive nanogels. Nanoscale 2018;10:469–79.
[57] Yan Q, Yuan JY, Cai ZN, Xin Y, Kang Y, Yin YW. Voltage-responsive vesicles based on orthogonal assembly of two homopolymers. J Am Chem Soc 2010;132:9268–70.
[58] Yuan ZY, Wang J, Wang YM, Zhong YJ, Zhang XS, Li L, Wang JY, Lincoln SF, Guo XH. Redox-controlled voltage responsive micelles assembled by noncovalently grafted polymers for controlled drug release. Macromolecules 2019;52:1400–7.
[59] Xu L, Wang H, Tian H, Zhang M, He J, Ni P. Facile construction of noncovalent graft copolymers with triple stimuli-responsiveness for triggered drug delivery. Polym Chem 2021;12:2152–64.
[60] Meng ZG, Sato K, Sutegana T, Oyaizu K, Ho CL, Xiang J, Feng YH, Lo YH, Nishide H, Wong WY. Metallopolyyne polymers with ferrocenyl pendant ligands as cathode-active materials for organic battery application. J Organomet Chem 2016;812:51–5.
[61] Cong GT, Zhou YC, Li ZJ, Lu YC. A Highly concentrated catholyte enabled by a low-melting-point ferrocene derivative. ACS Energy Lett 2017;2:869–75.
[62] Zhang CK, Qian YM, Ding Y, Zhang LY, Guo XL, Zhao Y, Yu GH. Biredox eutectic electrolytes derived from organic redox-active molecules: high-energy storage systems. Angew Chem Int Ed 2019;58:7045–50.
[63] Zhang QY, Cui XL, Zhang L, Luo SZ, Wang H, Wu YJ. Metal- and reagent-free highly selective anodic cross-coupling reaction of phenols. Angew Chem Int Ed 2015;54:5210–3.
[64] Mandai H, Fujii K, Yasuhara H, Abe K, Mitsudo K, Korenaga T, Suga S. Enantioselective acyl transfer catalysis by a combination of common catalytic motifs and electrostatic interactions. Nat Commun 2016;7:11297.
[65] Choi TL, Lee KH, Joo WJ, Lee S, Lee TW, Chae MY. Synthesis and nonvolatile memory behavior of redox-active conjugated polymer-containing ferrocene. J Am Chem Soc 2007;129:9842–3.
[66] Xiang J, Li XL, Ma Y, Zhao Q, Ho CL, Wong WY. Efficient flash memory devices based on non-conjugated ferrocene-containing copolymers. J Mater Chem C 2018;6:11348–55.
[67] Tan J, Li H, Hu XX, Abdullah R, Xi ST, Zhang LL, Zhao MM, Luo Q, Li YZ, Sun ZJ, Yuan Q, Tan WH. Size-tunable assemblies based on ferrocene-containing DNA polymers for spatially uniform penetration. Chem 2019;5:1775–92.
[68] Tan Z, Su H, Guo Y, Liu H, Liao B, Amin AM, Liu Q. Ferrocene-based conjugated microporous polymers derived from yamamoto coupling for gas storage and dye removal. Polymers (Basel) 2020;12:719.
[69] Wei Z, Wang D, Liu Y, Guo X, Zhu Y, Meng Z, Yu ZQ, Wong WY. Ferrocene-based hyperbranched polymers: a synthetic strategy for shape control and applications as electroactive materials and precursor-derived magnetic ceramics. J Mater Chem C 2020;8:10774–80.
[70] Mohamed MG, Meng TS, Kuo SW. Intrinsic water-soluble benzoxazine-functionalized cyclodextrin and its formation of inclusion complex with polymer. Polymer (Guildf) 2021;226:123827.
[71] Mohamed MG, EL-Mahdy AFM, Ahmed MMM, Kuo SW. Direct synthesis of microporous bicarbazole-based covalent triazine frameworks for high-performance energy storage and carbon dioxide uptake. Chempluschem 2019;84:1767–74.
[72] Mohamed MG, EL-Mahdy AFM, Meng TS, Samy MM, Kuo SW. Multifunctional hypercrosslinked porous organic polymers based on tetraphenylethene and triphenylamine derivatives for high performance dye adsorption and supercapacitor. Polymers (Basel) 2020;12:2426.
[73] Mohamed MG, Tsai MY, Wang CF, Huang CF, Danko M, Dai L, Chen T, Kuo SW. Multifunctional Polyhedral Oligomeric Silsesquioxane (POSS) based hybrid porous materials for CO_2 uptake and iodine adsorption. Polymers (Basel) 2021;13:221.
[74] Mohamed MG, Elsayed MH, Elewa AM, EL-Mahdy AFM, Yang CH, Mohammed AK, Chou HH, Kuo SW. Pyrene containing conjugated organic microporous polymers for photocatalytic hydrogen evolution from water. Catal Sci Technol 2021;11:2229–41.
[75] Mohamed MG, El-Mahdy AFM, Takashi Y, Kuo SW. Ultrastable conductive microporous covalent triazine frameworks based on pyrene moieties provide high-performance CO_2 uptake and supercapacitance. New J Chem 2020;44:8241–53.
[76] Nazeer AA, Husain AA, Samuel J, Rajendran N, Makhseed S. Hydroxyl-functionalized microporous polymer for enhanced CO_2 uptake and efficient super-capacitor energy storage. React Funct Polym 2020;154:104670.
[77] Samy MM, Mohamed MG, Kuo SW. Directly synthesized nitrogen-and-oxygen–doped microporous carbons derived from a bio-derived polybenzoxazine exhibiting high-performance supercapacitance and CO_2 uptake. Eur Polym J 2020;138:109954.
[78] Mohamed MG, Zhang X, Mansoure TH, El-Mahdy AFM, Huang CF, Danko M, Xin Z, Kuo SW. Hypercrosslinked porous organic polymers based on tetraphenylanthraquinone for CO_2 uptake and high-performance supercapacitor. Polymer (Guildf) 2020;205:122857.
[79] Paul A, Borrelli R, Bouyanfif H, Gottis S, Sauvage F. Tunable redox potential, optical properties, and enhanced stability of modified ferrocene-based complexes. ACS Omega 2019;4:14780–9.
[80] He X, Xie X, Wang J, Ma X, Xie Y, Gu J, Xiaoc N, Qiu J. From fluorene molecules to ultrathin carbon nanonets with an enhanced charge transfer capability for supercapacitors. Nanoscale 2019;11:6610–9.
[81] DeBlase CR, Silberstein KE, Truong TT, Abruña HD, Dichtel WR. β-ketoenamine-linked covalent organic frameworks capable of pseudocapacitive energy storage. J Am Chem Soc 2013;135:16821–4.
[82] Guo B, Yang Y, Hu Z, An Y, Zhang Q, Yang X, Wang X, Wu H. Redox-active organic molecules functionalized nitrogen-doped porous carbon derived from metal-organic framework as electrode materials for supercapacitor. Electrochim Acta 2017;223:74–84.
[83] Sun MQ, Wang GC, Yang CY, Jiang H, Li CZ. A graphene/carbon nanotube@π-conjugated polymer nanocomposite for high-performance organic supercapacitor electrodes. J Mater Chem A 2015;3:3880–90.
[84] Xu L, Shi R, Li H, Han C, Wu M, Wong CP, Kang F, Li B. Pseudocapacitive anthraquinone modified with reduced graphene oxide for flexible symmetric all-solid-state supercapacitors. Carbon N Y 2018;127:459–68.
[85] Khattak AM, Sin H, Ghazi ZA, He X, Liang B, Khan NA, Alanagh HR, Iqbal A, Li L, Tang Z. Controllable fabrication of redox-active conjugated microporous polymers on reduced graphene oxide for high performance faradaic energy storage. J Mater Chem A 2018;6:18827–32.
[86] Mohamed MG, Chen WC, EL-Mahdy AFM, Kuo SW. Porous organic/inorganic polymers based on double-decker silsesquioxane for high-performance energy storage. J Polym Res 2021;28:219.
[87] Samy MM, Mohamed MG, Kuo SW. Pyrene-functionalized tetraphenylethylene polybenzoxazine for dispersing single-walled carbon nanotubes and energy storage. Compos Sci Technol 2020;199:108360.
[88] Lee JSM, Wu TH, Alston BM, Briggs ME, Hasell T, Hub CC, Cooper AI. Controllable fabrication of redox-active conjugated microporous polymers on reduced graphene oxide for high performance faradaic energy storage. J Mater Chem A 2016;4:7665–73.
[89] El-Mahdy AFM, Kuo CH, Alshehri A, Young C, Yamauchi Y, Kim J, Kuo SW. Strategic design of triphenylamine- and triphenyltriazine-based two-dimensional covalent organic frameworks for CO_2 uptake and energy storage. J Mater Chem A 2018;6:19532–41.